

University of Dayton eCommons

Electro-Optics and Photonics Faculty Publications

Department of Electro-Optics and Photonics

5-2013

Nanowire Metal-Insulator-Metal Plasmonic Devices

Joseph W. Haus

University of Dayton, jhaus1@udayton.edu

Li Li

University of Dayton

Cong Deng

University of Dayton, cdeng1@udayton.edu

Nkorni Katte


Wilberforce University

Michael Scalora

Charles M. Bowden Research Center

See next page for additional authors

Follow this and additional works at: https://ecommons.udayton.edu/eop_fac_pub

 Part of the [Electromagnetics and Photonics Commons](#), [Nanoscience and Nanotechnology Commons](#), and the [Optics Commons](#)

eCommons Citation

Haus, Joseph W.; Li, Li; Deng, Cong; Katte, Nkorni; Scalora, Michael; de Ceglia, Domenico; and Vincenti, Maria Antonietta, "Nanowire Metal-Insulator-Metal Plasmonic Devices" (2013). *Electro-Optics and Photonics Faculty Publications*. 76.
https://ecommons.udayton.edu/eop_fac_pub/76

This Conference Paper is brought to you for free and open access by the Department of Electro-Optics and Photonics at eCommons. It has been accepted for inclusion in Electro-Optics and Photonics Faculty Publications by an authorized administrator of eCommons. For more information, please contact frice1@udayton.edu, mschlangen1@udayton.edu.

Author(s)

Joseph W. Haus, Li Li, Cong Deng, Nkorni Katte, Michael Scalora, Domenico de Ceglia, and Maria Antonietta Vincenti

Nanowire Metal-Insulator-Metal Plasmonic Devices

Joseph W. Haus¹, Li Li¹, Nkorni Katte², Cong Deng¹, Michael Scalora³, Domenico de Ceglia⁴ and Maria Antonietta Vincenti⁴

¹ *Electro-Optics Program, University of Dayton, Dayton, OH 45469-2951*

² *Electrical Engineering, Wilberforce University, Wilberforce, Ohio 45384*

³ *Charles M. Bowden Research Center, AMRDEC, RDECOM, Redstone Arsenal, AL 35898-5000*

⁴ *National Research Council - AMRDEC, Charles M. Bowden Research Center, Redstone Arsenal, AL 35898*

e-mail: jwhaus@udayton.edu

ABSTRACT

In this paper we theoretically study the responsivity of Metal-Insulator-Metal nanostructures to light illumination over a broad wavelength band (1 - 25 microns) and we examine the role of a local field enhancement and electrostatic field on the responsivity.

1. INTRODUCTION

The combination of photonic interactions in nanoplasmonic and quantum tunneling is opening a new vista for applications in energy harvesting and sensing. Exploiting the electron dynamics, whose response time is on a femtosecond scale, device band widths can approach 100's of THz and can provide a radical departure in performance of photonic devices [1-3].

In this paper we consider two metal nanoparticles that are embedded in a dielectric insulator and in close proximity to one another. The optical properties of dimers or (metal-insulator-metal (MIM) structures) have been studied in many publications [4-18]. The quantum properties of MIM nanostructures where the electrons are confined to the metals, but also are shared by tunneling through the insulator barrier, are to be examined here by including the electromagnetic fields around the dimer. In homostructured dimers where both metals and particle shapes are identical the symmetry of the potentials doesn't favor charge build-up on the average on one side or the other; however, in a heterostructured dimer the charge density can build up preferentially in one metal; the static charge will block additional charges from tunneling through the barrier and the local fields in the small gap between the metals will be reduced due to the electrostatic effect.

We illustrate our physical problem in Figure 1, which depicts a collection of MIM heterostructured nanorods with a vertical attitude. The image on the right labels the constituents of the structure. Different geometries are possible with the MIM nanorods at an oblique angle or even lying on the surface. The connections between the rod segments are not shown, but a conductive substrate would provide a reservoir of electrons to enable current flow. A top transparent and conductive layer (not shown) would be required to complete the circuit.

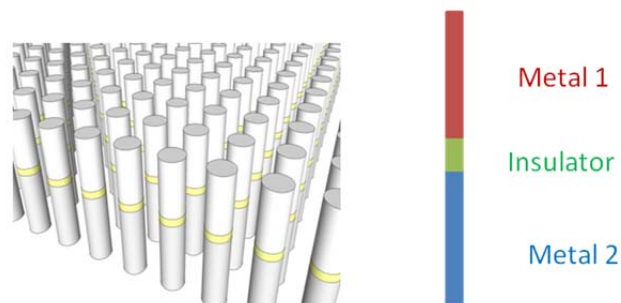


Figure 1: Illustration of a MIM tunneling structure.

2. QUANTUM TUNNELING ANALYSIS

We are interested in the problem of a free electron wave driven by an applied voltage and traveling across a region with a barrier potential. The current is a combination of the electron tunneling probability and the occupation densities of the energy levels. In this section we simplify the form of Schrödinger's equation to [19]

$$E\psi = -\frac{\hbar^2}{2m}\nabla^2\psi + V(x, y, z)\psi \quad (1)$$

There are many methods that could be applied to solve Schrödinger's equation; we used two methods to solve for the wave function: the transfer matrix method and the shooting method applying a finite difference technique. We tested both methods and applied the WKB method to validate our results as will be demonstrated below.

2.a. POTENTIAL FUNCTIONS

The potential in the Schrödinger equation incorporates the electronic material parameters. In the one electron equation the potential function is determined by two experimentally available coefficients. One parameter is the Work function, W , which is the minimum kinetic energy the electron requires to escape from the metal into the vacuum. The other parameter is the electron affinity, Φ , for the insulator to capture an electron at rest from the vacuum. These two parameters are listed for several metals and insulators in Table 1. The values are quoted in electron volts. The barrier height at the interface between the metal and insulator is given by

$$\varphi = W - \Phi \quad (2)$$

The potential barrier in the insulator region between two different metals is illustrated in Figure 2. The barrier height is measured from the Fermi energy, which is equal in both metals for the equilibrium case.

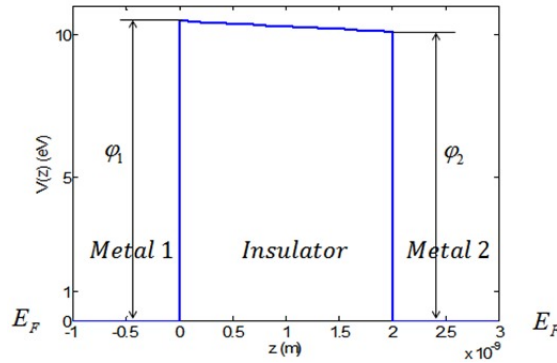


Figure 2: Illustration of the potential barrier in the MIM structure.

Most metals in the Table have work functions in a range from 4 to 4.7 eV; gold and platinum are interesting because their high work functions lead to correspondingly high potential barriers. The electron affinities in the Table also have relatively large values in the 3 to 4 eV range, but here also there are outliers, such as silica, which is less than 1 eV and as a result, the barrier heights are extremely large.

Table 1: Material property values for metals and insulators [11, 16, 20].

Metal	W (eV)	Insulator	Φ (eV)
Ag	4.26	Ta ₂ O ₅	3.83
Al	4.28	Al ₂ O ₃	1.78
Au	5.1	Cr ₂ O ₃	3.76
Cu	4.4	TiO ₂	3.9
Ti	4.33	Nb ₂ O ₅	4.23
W	4.55	SrTiO ₃	3.9
Nb	3.99	PbTiO ₃	3.1
Pt	5.65	BaZrO ₃	2.5
Sn	4.38	PbZrO ₃	3.2
Ta	4.25	ZrO ₂	2.5
NbN	4.7	Si ₃ N ₄	2.1
Cr	4.5	SiO ₂	0.9

Figure 3 is an illustration of the current flow when a voltage bias is applied. The voltage induced a current to flow in in one direction or the other by lowering the Fermi energy of one metal. The electrons tunnel through the barrier in one direction inducing a current in the opposite one. $T(E_z)$ is the quantum mechanical transmission function for the potential barrier. The average current depends on the quantum mechanical current weighted by the occupation of the electronic states on both side of the barrier.

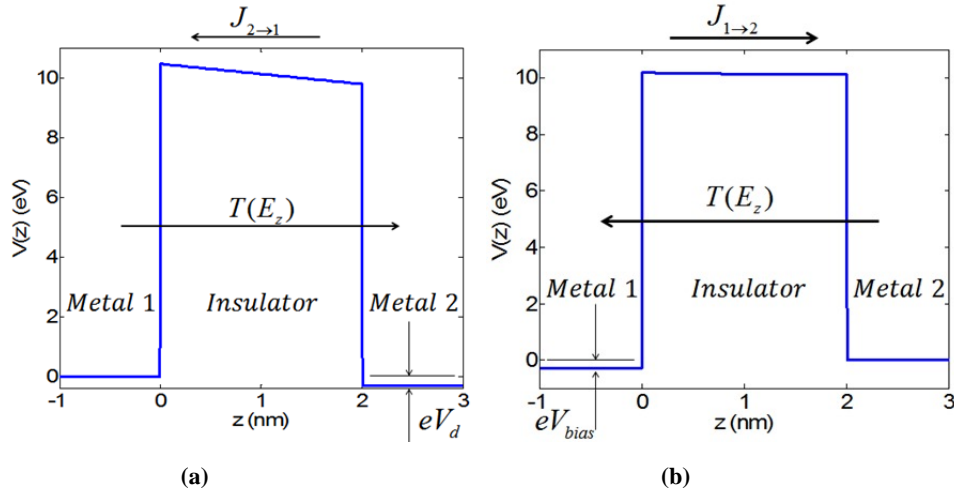


Figure 3: Energy band diagram of a MIM diode with different metal electrodes (Metal 1 and Metal 2). (a) Forward bias: electron tunneling from metal 1 to metal 2 is dominant, (b) Backward bias: A bias voltage applied in metal 1 result in electrons in metal 2 tunnels through the barrier into metal 1.

The expression for the 3D current density [21] for one direction of the applied voltage is

$$J^{3D} = 2e \frac{m^3}{h^3} \int_0^\infty dv_x v_z T(E_z) \iint (f(E) - f(E + eV_D)) dv_x dv_y, \quad (3)$$

where v_x and v_y are the transverse electron velocities and v_z is the longitudinal electron velocity, which is taken as positive for the direction of the potential barrier. The Fermi distribution functions are defined as:

$$f(E) = \frac{1}{e^{(E-E_F)/k_B T} + 1}, \quad (4)$$

where E_F is the Fermi energy, T the lattice temperature and k_B is Boltzmann's constant. Using the transformations

$$dv_x dv_y = d\theta v_r dv_r = \frac{1}{m} d\theta dE_r \quad \text{and} \quad v_z dv_z = \frac{1}{m} dE_z, \quad (5)$$

the total electron energy is defined as

$$E = E_r + E_z. \quad (6)$$

For constant values of E_z the lateral energy differential can be written as: $dE_r = dE$. The current density in 3D is transformed to a simplified form

$$J^{3D} = 4\pi e \frac{m}{h^3} \int_0^\infty dE_z T(E_z) \int_{E_z}^\infty (f(E) - f(E + eV_D)) dE. \quad (7)$$

2.b TRANSFER MATRIX TECHNIQUE

To solve for the current the first element to calculate the transmission function $T(E_z)$ [19, 21]. The Transfer Matrix technique (TMM) is easy to implement for any shape potential we solve Schrödinger's equation by slicing the potential into a set of slices, as in Figure 4. In each slice the potential is considered to be constant. The incident wave has an amplitude A , while the outgoing wave has a complex amplitude C and the reflected wave has an amplitude B .

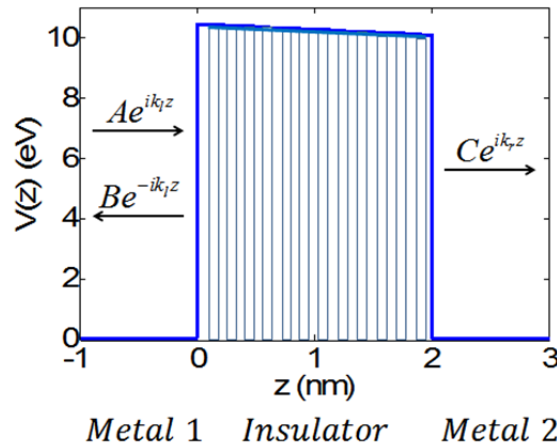


Figure 4: A illustrative electronic Potential (blue) for NbN/ Nb₂O₅/ Nb with a barrier region that is characterized by a linear slope. The Fermi energy is taken as 10 eV. The sub-regions of constant potential are indicated by boxes of small width and heights that are adjusted to the potential height in the region.

The transmission for a potential is plotted in Figure 5 for a number of energies on a logarithmic scale. The transmission coefficient changes by more than 9 orders of magnitude. The TMM and shooting method are compared as is the WKB result shown on the plot [19].

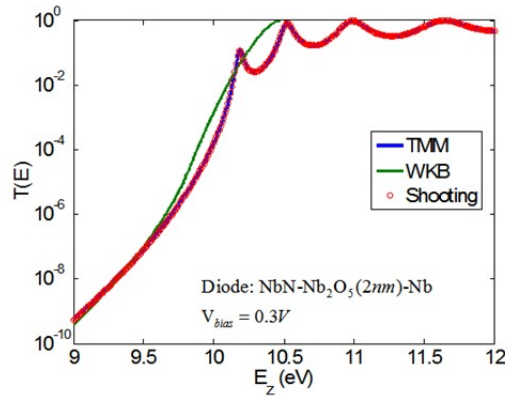


Figure 5: The tunneling probability as a function of energy for the energy diagram of MIM diode: NbN/Nb₂O₅/Nb. The solution is plotted for both TMM (blue) and shooting method (red). The WKB approximation [19] is shown for comparison (green).

For completeness a wave function is plotted in Figure 6 below where we plot for an energy $E_z = 12$ eV, which lies above the potential barrier. In the barrier region (0,2nm) the amplitude and the spatial oscillation frequency change. The reflected wave interferes with the incident wave leading to a doubling of the spatial oscillation frequency.

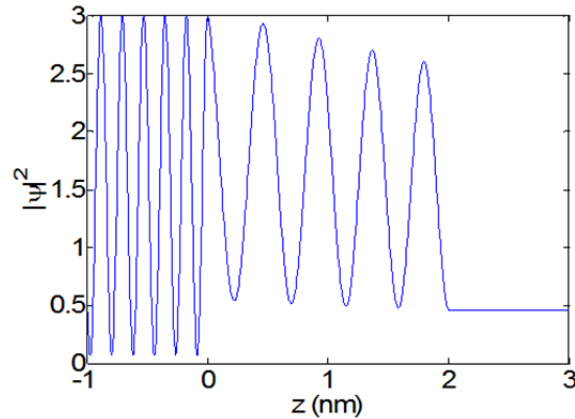


Figure 6: The wave function magnitude plotted versus position for the energy of 12 [eV] for NbN/Nb₂O₅/Nb.

3. TUNNELING CURRENT IN CONFINED GEOMETRIES

We derive a tunneling current with lateral confinement of the electrons in a nanowire (1D) or nanoslab (2D) geometry. The confinement will have an effect on the current density and we wanted to quantify the effects of lateral confinement. The nanowire is confined in both lateral dimensions and the nanoslab is confined in one lateral dimension.

3.a CURRENT DENSITY 2D

Confine the x dimension to a width d_x . The energy is quantized due to the confinement by the expression

$$E_x = \frac{h^2}{8m} \left(\frac{n_x}{d_x} \right)^2, \quad (8)$$

We posit that the corresponding 2D current density is

$$J^{2D} = 2e \frac{m^2}{h^2} \int_0^\infty dv_z v_z T(E_z) \frac{1}{d_x} \sum_{n_x=1}^\infty \int (f(E) - f(E + eV_D)) dv_y . \quad (9)$$

The total energy is

$$E = E_z + \frac{h^2 \left(\frac{n_x}{d_x} \right)^2}{8m} + \frac{mv_y^2}{2} . \quad (10)$$

The expression for J^{2D} is chosen because it yields the 3D result in the limit d_x goes to infinity. To show this result note that the differential of the wave vector x-component is

$$\Delta k_x = \frac{\pi}{d_x} , \quad (11)$$

and the velocity differential is

$$\Delta v_x = \frac{h}{2\pi m} \Delta k_x . \quad (12)$$

Extending the sum to include negative and positive momenta and making the above transformation to velocity space we have the sum replaced by an integral

$$\frac{1}{d_x} \sum_{n_x=1}^\infty \rightarrow \frac{m}{h} \int_{-\infty}^\infty dv_x . \quad (13)$$

Inspection will show that when this is inserted into J^{2D} that it is precisely equal to J^{3D} .

3.b CURRENT DENSITY 1D

Deriving the expression for the 1D current density is straightforward and can be done by extending the analysis presented in the previous section. The 1D current density is

$$J^{1D} = 2e \frac{m}{h} \int_0^\infty dv_z v_z T(E_z) \frac{1}{d_x d_y} \sum_{\substack{n_x=1 \\ n_y=1}}^\infty (f(E) - f(E + eV_D)) . \quad (14)$$

The total energy is

$$E = E_z + \frac{h^2 \left(\frac{n_x}{d_x} \right)^2}{8m} + \frac{h^2 \left(\frac{n_y}{d_y} \right)^2}{8m} . \quad (15)$$

These can be applied to determine the current density in a similar fashion to the 3D case.

3.c RESULTS COMPARING CONFINED CURRENT DENSITIES

The 2D and 1D results are constructed to reduce to the 3D result in the limit of large dimensions. In the figure below four cases are exhibited. The current densities are plotted on a logarithmic (base 10) scale in Figures 7. The current density is lower for the confined electron cases. The 1D shows a trend toward lower current density than the 2D case. This establishes a consistent result for the confined electron geometry. For $d_x=d_y=100$ nm the current densities for the 2D and 1D geometries are within 2% and 4%, resp. of the 3D case.

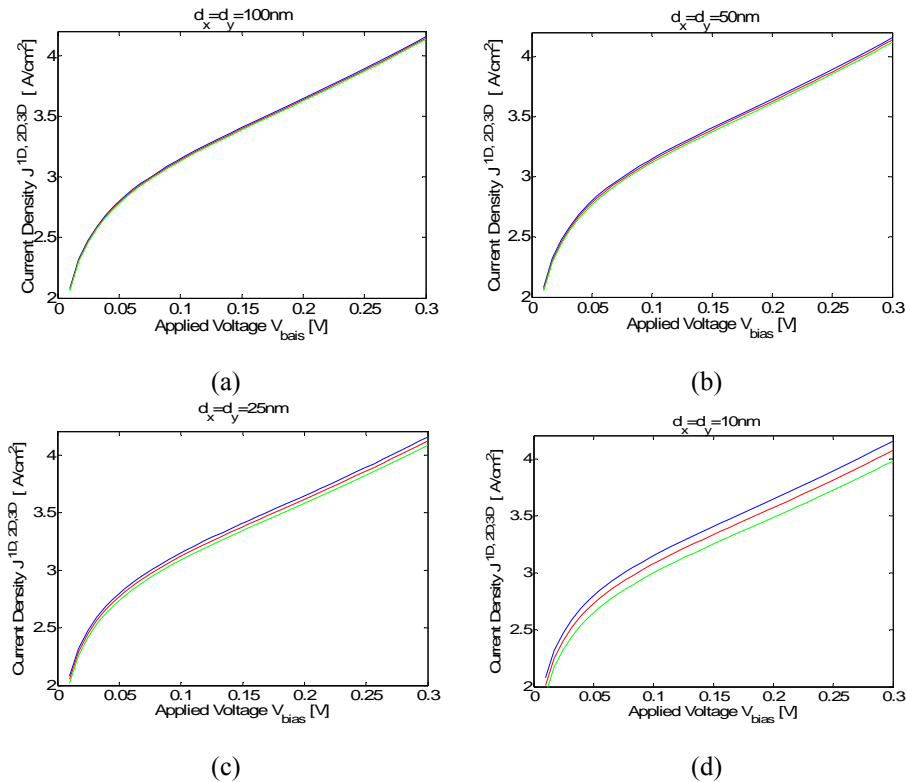


Figure 7: Applied voltage as a function of current density for the case of the MIM diode design NbN/ Nb₂O₅/ Nb with gap=2nm. Color code: blue: J^{3D}, red: J^{2D} and green: J^{1D}. The lateral confinement parameters are: (a) d_x and/or $d_y=100$ nm, (b) d_x and/or $d_y=50$ nm, (c) d_x and/or $d_y=25$ nm, (d) d_x and/or $d_y=10$ nm.

4. DARK CURRENT

In this section we briefly present a few calculated MIM dark currents using the 3D expression for the current given in Eq. (7). In Figure 8 we plotted three illustrative examples of the dark tunneling current versus voltage bias (positive and negative voltages) and insulator gap thickness. There is an asymmetry in the positive and negative bias currents due to the different internal bias create by the different work functions of the constituent metals. The MIM heterostructures reveal a diode current characteristic due to the asymmetric potential barrier from the work functions. We consider the cases Ag/TiO₂/Ti, Al/Nb₂O₅/Nb and Au/Nb₂O₅/Nb. All material parameters for the calculations are taken from Table 1.

The trends in all the dark current are generally the same. For a fixed applied voltage, the dark tunneling current decreases with increasing gap thickness; in other words it is more difficult for the electron to tunnel through a thicker barrier. Also for a fixed gap thickness, a higher dark tunneling current obtained by increasing the applied voltage. It is not readily apparent in these figures, but the dominant (forward or backward) current for a given magnitude of bias is not the same for all bias voltages. The asymmetry of two oppositely biased MIM nanostructures is determined only by differences between two work functions of metals and the barrier thickness. The opposite

current amplitudes may cross one another at a bias voltage which affects the asymmetry in the net rectified diode current.

For the top two MIM diode cases in Figure 8 the dark tunneling current results show a modest asymmetry (1 order of magnitude difference) of forward and backward current flow at the largest applied bias voltages. But in the bottom case with gold we have a tremendous forward-to-backward current ratio of several orders of magnitude. It is noted that gold has a large work function compared with many other metals in Table 1 and the current densities at all bias voltage values at the same insulator gap thickness are orders of magnitude lower than many other MIM examples.

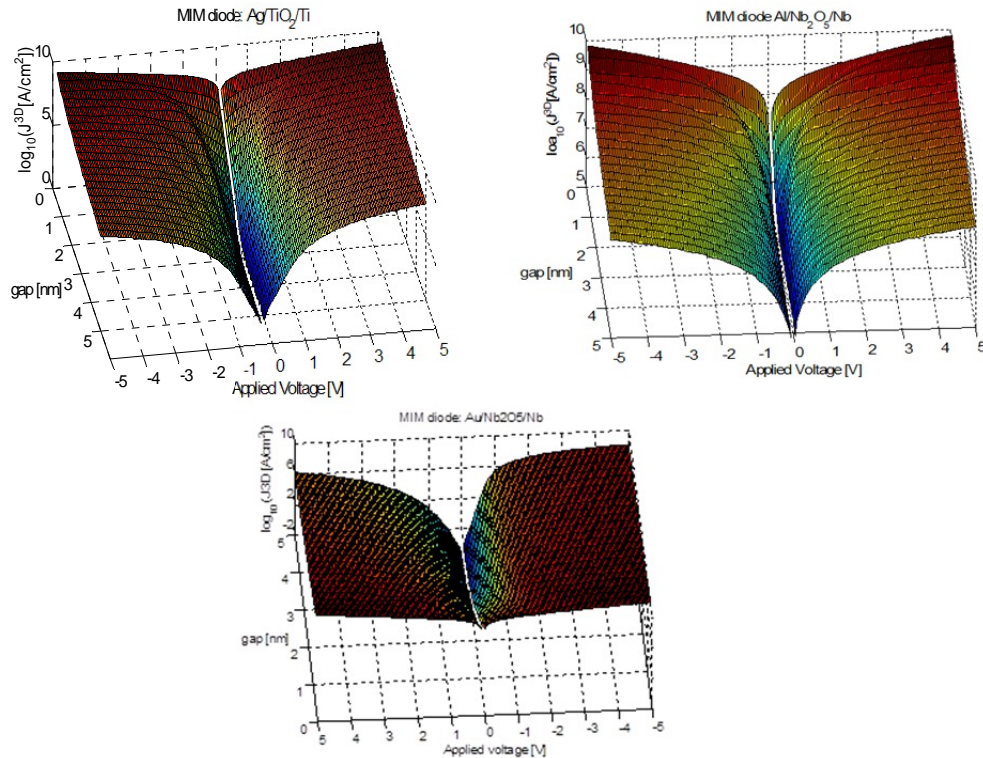


Figure 8: The calculated tunneling current curve versus. applied voltage and different gap thickness for Ag/TiO₂/Ti MIM diode (Top left), Al/Nb₂O₅/Nb MIM diode (Top right) and Au/Nb₂O₅/Nb MIM diode (bottom). The tunneling current curve calculated by the TMM.

5. ILLUMINATED MIM STRUCTURES

The Hamiltonian for the electromagnetic field that affects the tunneling across the barrier is given by [23]

$$H(t) = H_0 + V_\omega \cos(\omega t). \quad (16)$$

The last term on the right hand side is the ac voltage, V_ω , across insulator gap of the MIM structure. The time-dependent contribution to the Hamiltonian is modeled as a voltage across the MIM structure. The potential V_ω is related to the strength of the electric field. The field in the gap can increase the coupling which is accomplished by incorporating plasmonic effects into the MIM design. When the electric field parallel to the current flow direction is denoted as E_ω , the voltage is given by

$$V_\omega = E_\omega d, \quad (17)$$

where d is the thickness of the insulating gap. The dc tunneling current in their theory truncating an infinite series to just three terms is [23-25]

$$J^{dc}(V_{bias}) = J_1^2(\alpha) J^{3D}(V_{bias} + \frac{\hbar\omega}{e}) + J_{-1}^2(\alpha) J^{3D}(V_{bias} - \frac{\hbar\omega}{e}) + J_0^2(\alpha) J^{3D}(V_{bias}). \quad (18)$$

where $\alpha = eV/\hbar\omega$. Note that to calculate the illuminated current we only need to know the dark current at biases that are shifted up or down by a “photon voltage” $\pm \hbar\omega/e$. The result in Eq. (18) is plotted in Figure 9 and it shows how the current is generally increased with larger alpha parameter. In other words with photon assisted tunneling more current is generated as the field gets stronger.

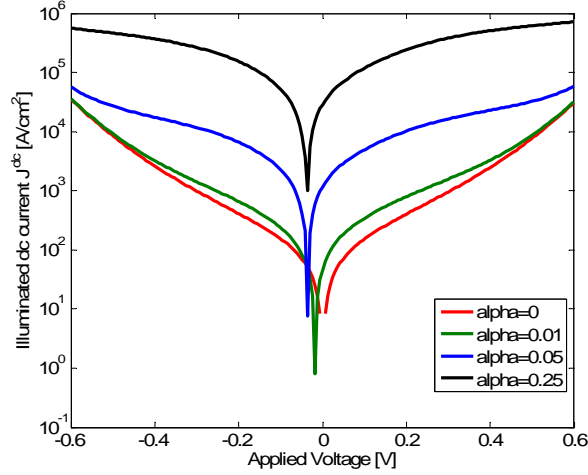


Figure 9: Illuminated dc current versus applied voltage for MIM diode Ag/TiO₂/Ti under small incoming field. The thickness is fixed at 2nm as an example and the photon energy is 1.4 eV. The red curve shows when alpha is equal to zero corresponding to dark current.

The change in the dc current due to the illumination is the difference between the $\alpha = 0$ and $\alpha \neq 0$ currents. For small α change in the dc current is

$$\Delta J^{dc}(V_{bias}) = \frac{\alpha^2}{4} [J^{3D}(V_{bias} + \frac{\hbar\omega}{e}) - 2J^{3D}(V_{bias}) + J^{3D}(V_{bias} - \frac{\hbar\omega}{e})]. \quad (19)$$

The quantum mechanical ac current has all the harmonic components of the applied field. The fundamental frequency current after similarly expanding Bessel function in lowest-order is

$$J^\omega = \frac{\alpha}{2} [J^{3D}(V_{bias} + \hbar\omega/e) - J^{3D}(V_{bias} - \hbar\omega/e)]. \quad (20)$$

The weak-field, MIM diode responsivity expression is given by [11, 16]:

$$R = \frac{\Delta J^{dc}}{J^\omega} \frac{2e}{\alpha \hbar\omega} = \frac{e}{\hbar\omega} \left[\frac{J^{3D}(V_{bias} + \hbar\omega/e) - 2J^{3D}(V_{bias}) + J^{3D}(V_{bias} - \hbar\omega/e)}{J^{3D}(V_{bias} + \hbar\omega/e) - J^{3D}(V_{bias} - \hbar\omega/e)} \right]. \quad (21)$$

6. ELECTRIC FIELD ENHANCEMENT

Surface plasmon resonance for a single ellipsoidal particle is an analytically solved problem. We use the results for prolate spheroids here. The absorption spectra for different particle geometries (the major and minor axes ratio is changed) are shown below for the field along two different principal axes. In the spherical case the resonance frequencies are degenerate and they separate further as the axes are changed. One case of the field squared relative to the applied field is shown on the right. The field is enhanced about ten times near the end of the prolate spheroid.

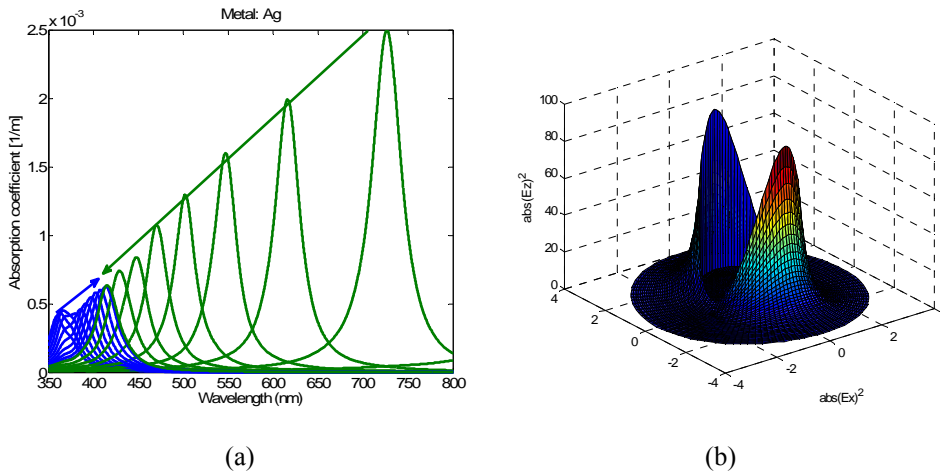


Figure 10: (a) Absorption as a function of wavelength (350nm~800nm) for different particle shape from spherical to aspect ratio 10:1. (b) Local electrical field distribution squared around a prolate spheroidal shaped particle at the wavelength of the surface plasmon resonance (x,z) plane.

However, SPR is not the only mechanism for increasing the field in the gap between two spheroids. Electrostatic charges at the tips of the spheroids will also create enhanced fields. The electrostatic mechanism is illustrated in Figures 11. The applied field is nominally taken as 1 V/m. In Figure 11(a) the field is strongly confined to the gap region between the two nanowires. A close up of the gap in Figure 11(b) shows that the field is concentrated to a narrow region and it is increased by about 70 times over the value of the applied field.

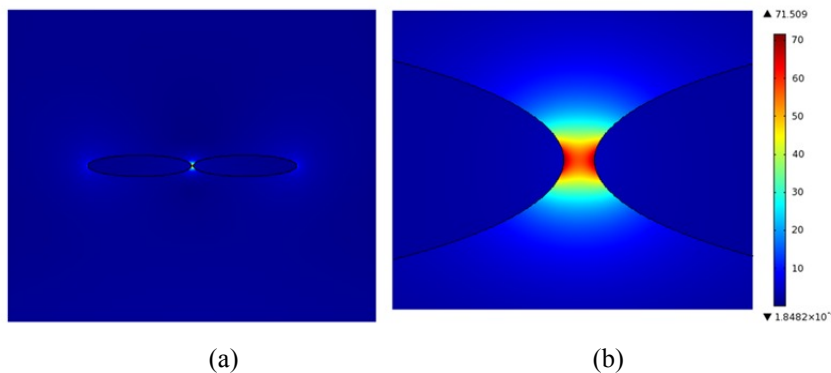


Figure 11: Field intensity in the vicinity of two elliptical cross-section nanowires with major and minor axes 50nm and 10 nm respectively. The gap is 1.9 nm. (a) two elliptic cross sections of the nanowires with field strength indicated in color. (b) a close up of the gap region with field magnitude shown on the bar.

The map of the field enhancement in the gap versus wavelength and gap size for a silver-tantalum dimer is shown in Figure 12. The field is strongest for the smallest gaps with an enhancement of more than two orders of magnitude. The value drops rapidly for gap sizes in the 2-3 nm range the enhancement ranges from 10 to 80 times the applied field.

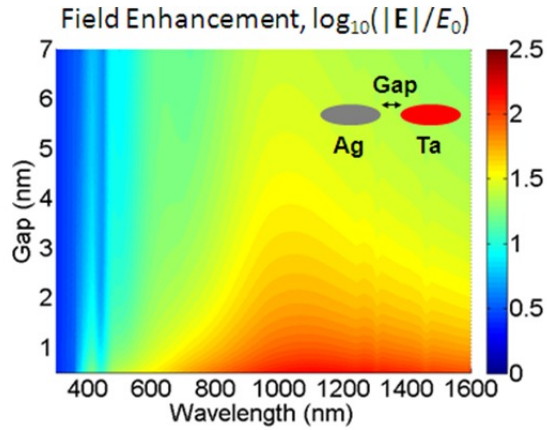


Figure 12: Plot of the field intensity versus wavelength for the maximum field as a function of wavelength.

The enhancement for the above case is somewhat modest given the alpha parameter values will still be small. However, for two prolate spheroids brought close together the field enhancement in the gap region will be much larger. The field enhancement will be the subject of future studies to discover the band width and magnitude of the effect.

6.a OPTICAL VOLTAGE

For solar energy we have to harvest the energy available from the sun. The average irradiance from the sun is about 125 W/m^2 . Consider a solar concentrator that focuses light with an aperture radius of 10 cm to a spot size of 100 microns. The irradiance at the focus is: $1.25 \times 10^8 \text{ W/m}^2$. The corresponding electric field is $E = \sqrt{2I / \epsilon_0 c} = 3.069 \times 10^5 \text{ V/m}$. Therefore the voltage across the MIM junction for an insulator of thickness 2 nm is $V = 0.6138 \text{ mV}$. A small voltage indeed!

In comparison with the photon energy per electron charge at a wavelength of 1 micron the result is $E_{\text{photon}} = \hbar\omega / e = 1.24 \text{ V}$. As a result the parameter in the Tien and Gordon theory [23] is small $\alpha = V / E_{\text{photon}} = 4.94 \times 10^{-4}$. The Bessel functions appearing in the expression for the current will be correspondingly tiny. For this case $J_1(\alpha)^2 = 6.1 \times 10^{-8}$.

The plasmonic resonance can increase the local field in the junction region by several orders of magnitude at least over a small range of wavelengths. Consider the cases of nanospheres or nanowires that are within a few nanometers of one another. Publications show enhancements of 5 to 10 orders of magnitude. The α parameter can be much larger than unity in these cases. A field enhanced by four value orders of magnitude yields $\alpha = V / E_{\text{photon}} = 4.94$ and the Bessel function $J_1(\alpha)^2 = 0.103$. This is an increase by nearly seven orders of magnitude.

7. RESPONSIVITY RESULTS

Without applied voltage and with applied voltage, the calculated responsivity as a function of gap and wavelength (λ) for several MIM diodes are shown in Figures 13 and 14. Further cases are studied in Ref. [26]. The wavelength range we chose is from 1 to 25 microns. The calculation of the illuminated current is simplified because we can calculate the dark current once and use the data as a look-up table for exploring the effect of various parameter values on the responsivity, Eq. (21), for the MIM photodiode. We used the data of dark current J^{3D} for MIM diodes discussed in a previous section.

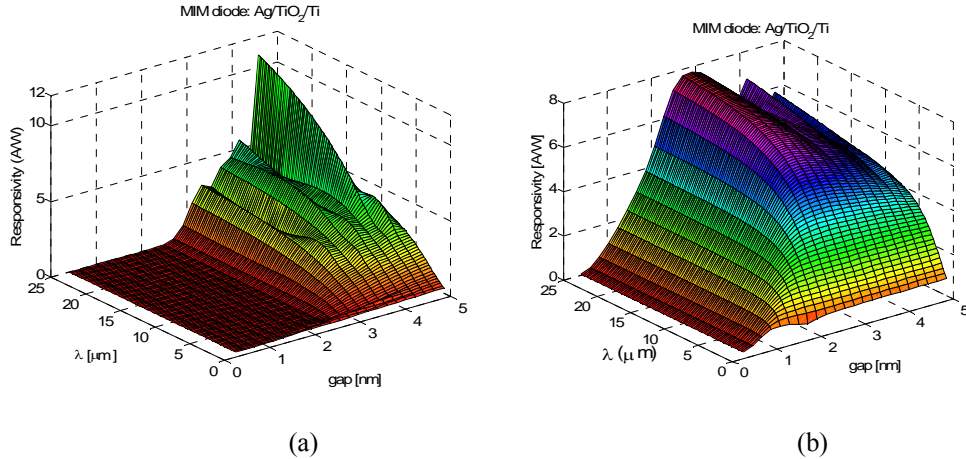


Figure 13: Responsivity versus wavelength and gap for MIM diode Ag/TiO₂/Ti under small incoming field. (a): Zero bias applied. (b): 0.3V bias applied.

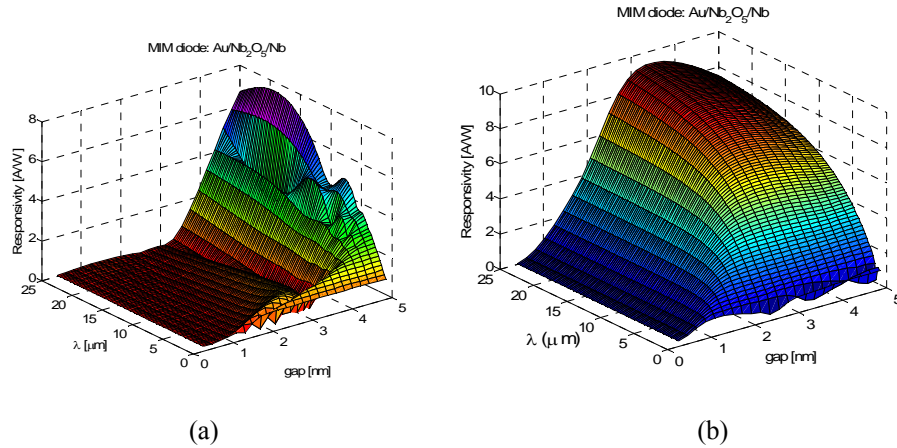


Figure 14: Responsivity versus wavelength and gap for MIM diode Au/Nb₂O₅/Nb under small incoming field. (a) Zero bias applied. (b) 0.3V bias applied.

The responsivity without a dc bias voltage applied is weak when the gap is smaller. The currents for thicker barriers will be quite small even though the value of the responsivity may be large. By applying a bias the responsivity generally increases at barrier thicknesses around 2nm and at shorter wavelengths it reaches the quantum limit given by $R_{quantum} = e/\hbar\omega$. In other words one electron is produced by one photon. The change of the responsivity for $d=4\text{ nm}$ in a Ag/TiO₂/Ti diode with applied voltage is shown in Figure 15. The case with a bias voltage shows improved responsivity with the shorter wavelengths at the quantum limit and longer wavelengths at a higher plateau value.

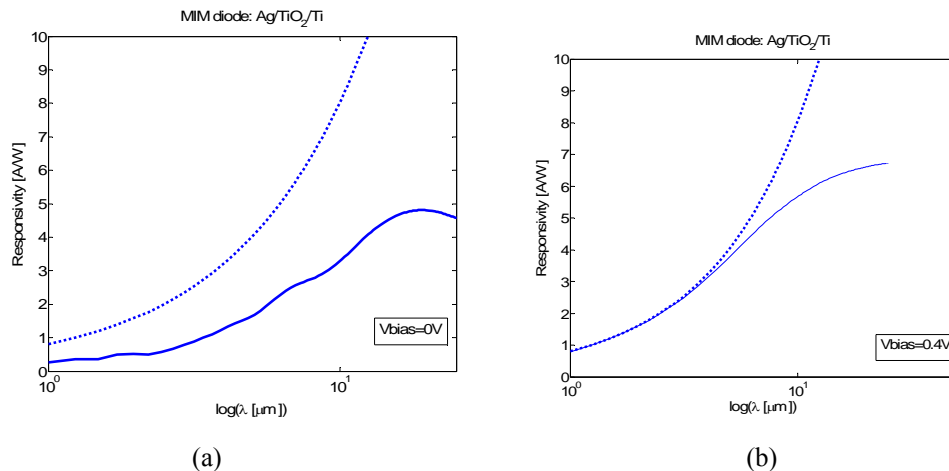


Figure 15: (a) Responsivity vs. log scale plot of wavelength for MIM diode Ag/TiO₂ (4nm)/Ti under small incoming field, with $V_{\text{bias}}=0\text{V}$. Quantum efficiency limit (dot). (b) Responsivity vs. log scale plot of wavelength for MIM diode Ag/TiO₂ (4nm)/Ti under small incoming field, with $V_{\text{bias}}=0.4\text{V}$. Quantum efficiency limit (dotted line).

8. CONCLUSIONS

We envision MIM diode applications that integrate the quantum and photonic aspects in the areas of energy harvesting and broad band and ultrafast photodetectors. We also propose that nonlinear optical experiments on harmonic generation and stimulated Raman scattering using MIM nanostructures extending to ultraviolet wavelengths. In our work we have explored using noble metals with other metals to enhance the field in the gap region of the heterostructured dimers. Besides the usual localized surface plasmon field enhancement mechanism, there is an electrostatic field generated enhancing the field across the insulator junction. We find that the electron tunneling current in MIM structures is enhanced by several orders of magnitude by using a metal in the design with a local surface plasmon resonance and large electrostatic field. Noble metals like gold, silver and copper possess resonances in the visible wavelength region that are shifted to the IR regime by changing the particles shape. The specific resonance wavelength is controlled by designing the shape of the particles. The electromagnetic resonance can be moved across the visible region and into the IR providing sufficient tailoring to cover the greater portion of the solar spectrum. The electrostatic effect is determined by the work functions and electron affinity of the individual materials.

ACKNOWLEDGMENTS

This research was performed while the authors J. W. Haus, M. A. Vincenti and D. de Ceglia held a National Research Council Research Associateship award at the U.S. Army Aviation and Missile Research Development and Engineering Center. Thanks are also extended to Prof. Concita Sibilia of the University of Rome - La Sapienza for discussions and hospitality while JWH was in Rome.

REFERENCES

- [1] C. Fumeaux, W. Herrmann, F. K. Kneubühl and H. Rothuizen, "Nanometer thin-film Ni–NiO–Ni diodes for detection and mixing of 30 THz radiation," *Infrared Phys. Technol* **39**, 123 (1998).
- [2] M. R. Abdel-Rahman, F. J. Gonzalez, G. Zummo, C. F. Middleton and G. D. Boreman, "Antenna-coupled MOM diodes for dual-band detection in MMW and LWIR," *Proc. SPIE* **5410**, 233 (2004).
- [3] P. C. Hobbs, R. B. Laibowitz, F. R. Libsch, N. C. LaBianca and P. P. Chiniwalla, "Efficient waveguide-integrated tunnel junction detectors at 1.6 μm ," *Opt Express* **15**, 16376 (2007).
- [4] M. Nagae, "Response time of metal-insulator-metal tunnel junctions," *Jpn. J. Appl. Phys.* **11**, 1611 (1972).
- [5] W. Tantraporn, "Electron current through metal-insulator-metal sandwiches," *Solid-State Electronics* **7**, 81 (1964).

- [6] L. O. Hocker, D. R. Sokoloff, V. Daneu and A. Javan, "Frequency mixing in the infrared and far-infrared using a metal-to-metal point contact diode," *Appl. Phys.*, **12**, 401 (1968).
- [7] R. L. Bailey, "A proposed new concept for a solar energy convertor," *J. Eng. Power* **94**, 73 (1972).
- [8] A. Sanchez, C. F. Davis, K. C. Liu and A. Javan, "The MOM tunneling diode: theoretical estimate of its performance at microwave and infrared frequencies," *J. Appl. Phys.* **49**, 5270 (1978).
- [9] C. Fumeaux, W. Herrmann, F. K. Kneubühl and H. Rothuizen. "Nanometer thin-film Ni–NiO–Ni diodes for detection and mixing of 30 THz radiation," *Infrared Phys. Tech.* **39**, 123 (1998).
- [10] M. Sarehraz, "Novel rectenna for collection of infrared and visible radiation," University of South Florida, Ph.D. Thesis (2005).
- [11] B. J. Eliasson, "Metal–insulator–metal diodes for solar energy conversion," University of Colorado at Boulder, Ph.D. Thesis (2001).
- [12] M. Dagenais, K. Choi, F. Yesilkoy, A. N. Chryssis and M. C. Peckerar, "Solar spectrum rectification using nano-antennas and tunneling diodes," *Proc. SPIE* **7605**, 76050E (2010).
- [13] S. Bhansali, S. Krishnan, E. Stefanakos and D. Y. Goswami, "Tunneling junction based rectenna - a key to ultrahigh efficiency solar/thermal energy conversion," *AIP Conf. Proc.* **1313**, 79 (2010).
- [14] E. Laux, C. Genet, T. Skauli, and T. W. Ebbesen, "Plasmonic photon sorters for spectral and polarimetric imaging," *Nat. Photonics* **2**, 161 (2008).
- [15] S. Grover, O. Dmitriyeva, M. J. Estes and G. Moddel, "Traveling-wave metal/insulator/metal diodes for improved infrared bandwidth and efficiency of antenna coupled rectifiers," *Nanotechnol IEEE Trans.* **9**,716 (2010).
- [16] S. Grover and G. Moddel, "Engineering the current–voltage characteristics of metal–insulator–metal diodes using double-insulator tunnel barriers," *Solid-State Electronics* **67**, 94 (2012).
- [17] S. Grover and G. Moddel, "Applicability of metal/insulator/metal (MIM) diodes to solar rectennas," *IEEE J. of Photovoltaics* **1**,78 (2011).
- [18] O. Imafidon, S. Georgakopoulos, P. K. Vabbina and N. Pala. "Multifunctional nanodevices for energy harvesting in unconventional spectral ranges," *Proc. SPIE* **7679**, 76792L (2010).
- [19] H. Kroemer, [*Quantum Mechanics*], 3rd ed., (Prentice-Hall Inc., NJ, 1994).
- [20] J. Robertson, "Band offsets of wide-band-gap oxides and implications for future electronic devices," *J. Vac. Sci. Technol. B* **18**, 1785 (2000).
- [21] J. G. Simmons, "Electric Tunnel Effect between Dissimilar Electrodes Separated by a Thin Insulating Film," *J. Appl. Phys.* **34**, 2581 (1963).
- [22] A. K. Ghatak, K. Thyagarajan and M. R. Shenoy "A novel numerical technique for solving the one-dimensional Schrödinger equation using matrix approach-application to quantum well structures," *IEEE J. Quant. Electron.* **24**, 1524 (1988).
- [23] P. K. Tien and J. P. Gordon, "Multiphoton Process Observed in the Interaction of Microwave Fields with the Tunneling Between Superconductor Films," *Phys. Rev.* **129**, 647 (1963).
- [24] J. R. Tucker and M. F. Millea, "Photon detection in nonlinear tunneling devices," *Appl. Phys. Lett.* **33**, 611 (1978).
- [25] J. R. Tucker and M. J. Feldman, "Quantum detection at millimeter wavelengths," *Rev. Mod. Phys.* **57**, 1055 (1985).
- [26] Li Li, "Study of Metal-Insulator-Metal Diodes for Photodetection," M.S. Thesis, University of Dayton (2012).